Surface Energy Balance of High Altitude Glaciers in the Central Andes: the Effect of Snow Penitentes

Javier G. Corripio[1] and Ross S. Purves[2]

[1] Centre d'Etudes de la Neige, Météo France
[2] Department of Geography, University of Zürich, Switzerland

Introduction

The Dry Central Andes stretching from latitude $31°$ S to $35°$ S are climatic deserts, yet they support rich agriculture and large urban centres thanks to melt water from glaciers and snow covered mountains. Most of the agriculture of the Chilean Central Valley is irrigated (Schwerdtfeger 1976), and all drinking water for Santiago de Chile, with over five million inhabitants (one third of the population of Chile), comes from water reservoirs fed by snow and ice melt during the summer. On the Argentinian side of the Andes, with barely 180 mm of annual precipitation, the provinces of Mendoza (population over 1.5 million) and San Juan are the country's main wine producers and the region has rich agricultural farms. This production is only possible thanks to a well developed irrigation system making efficient use of the summer melt water from the Cordillera. The contrast between the desert natural vegetation and the lush green of the cultivated farms is evident over the whole province, stressing the vital role of the mountains as "water towers of the world for the 21st Century." (Liniger et al. 1998)

In this paper we present results from a field campaign and associated modelling, comparing the components of energy balance in this area with that of Alpine basins and presenting low cost remote sensing techniques suitable for use in a region where access is difficult and expensive. Particular attention is given to penitentes: surface ablation forms that are common on most glaciers of the Central Andes at high altitude, and have an important effect on the energy and mass balance of the snow cover. The relative importance on snow ablation and therefore on water resources will be addressed

Site of study

The areas of study are two glaciers near the latitude of Santiago de Chile (see map in figure 1): the Juncal Norte glacier near the border with Argentina and south of

the Portillo pass, and the Loma Larga glacier on the headwaters of the Maipo river. The characteristics of the upper basins containing the glaciers are summarised in table 1. An automatic weather station (AWS) was installed on the snow surface and collected data from 30 November to 11 December 2000 on Juncal and from 22 January to 24 February 2001 on Loma Larga. The instruments were carried with the help of local arrieros and mules from the nearest road to the base camp near the glacier snout, and then by the researchers to the glacier location.

Table 1. Main characteristics of the upper catchment of the glaciers under study.

	cartchment 1	catchment 2
Name of the basin	Juncal Norte	Loma Larga
Mountain Range	Andes	Andes
Elevation range of upper catchment	2900-6100	2900-5404
Elevation range of individual sites	3335	4667
Latitude and longitude	32.98°S, 69.95°W	33.69°S, 70.00°W
Area in km^2	21	18
% glacierized	39	66
Geology	Andesites, trachytes and basalts	Andesites, trachytes and basalts
Vegetation type (dominant)	Alpine xerophytic, desert	Alpine xerophytic, desert
Mean Q at catchment outlet	Unknown	Unknown
Mean N	3060 h	3220 h

Climatic setting

Along the 33° S parallel, annual average precipitation ranges from 459 mm in Valparaiso (33.02° S, 71.63° W, 41 m a.s.l.) on the Pacific coast, to 356 mm in Santiago (33.45° S, 70.70° W, 520 m a.s.l.) and 180 mm in Mendoza (32.89° S, 68.83° W, 769 m a.s.l.), on the Argentinian side of the Cordillera (Schwerdtfeger 1976). In this region climatic seasonality is well defined, with dry summers and most of the precipitation occurring during the winter months. The southwestern Pacific perturbations reach the mountains only during the winter, producing variable precipitation, which is always in the form of snow at altitude (Lliboutry 1965). During the summer the weather is extremely dry and stable, characterised by the constant presence of the Pacific anticyclone over the region. In fact, less than 1% of the annual total precipitation is recorded during the December–February period. Frontal activity is infrequent, and precipitation, both on the mountain range and in the lee of the mountains, is mainly due to convective activity (Schwerdtfeger 1976).

The synoptic situation during fieldwork is summarised in figure 2, which shows the surface sea level pressure over South America. As indicated by Lliboutry (1998), a belt of stationary high pressure extends across the Pacific Ocean west of South
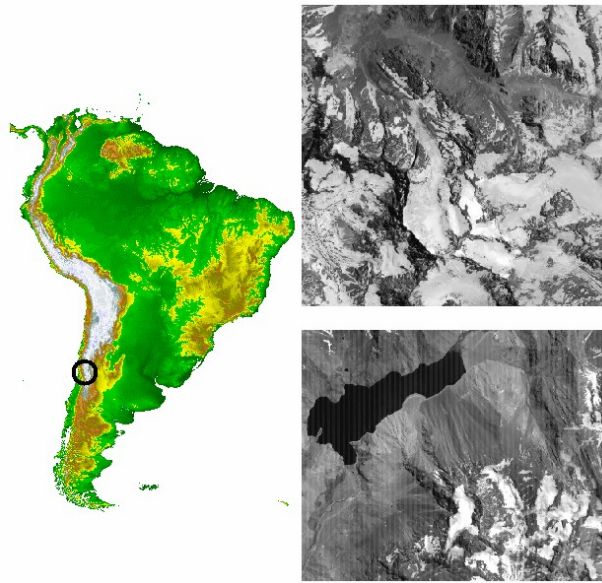
Fig. 1. The area of study in the Chilean Andes, about 33° S 70° W. In the right upper photograph Juncal Norte is the main glacier at the lower centre of the image, flowing north. Loma Larga is on the lower right corner of the lower image, in the opposite corner is the Yeso dam, the main water reservoir for Santiago de Chile. Map source: GLOBE project, NOAA, NGDC. Images from Aster: asterweb.jpl.nasa.gov
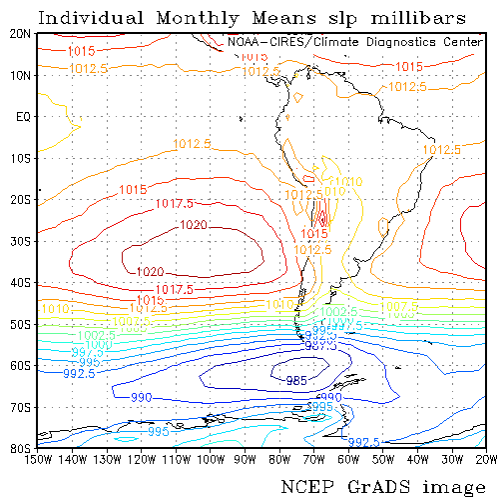

Fig. 2. Surface sea level pressure averaged from December 2000 to February 2001. The image is a visualisation of NCEP/NCAR reanalysis data provided by the NOAA-CIRES Climate Diagnostics Center, Boulder, Colorado, from their web site at http://www.cdc.noaa.gov/ .

America, preventing intrusion of moisture-laden air masses to the continent. This stationary anticyclone is also responsible for a minimum in relative humidity over central Chile during the summer months. The same reanalysis data show a mean relative humidity of 35% on the western coast of Chile, at about 33 °latitude south, the minimum for the southern hemisphere outside Antarctica. The solar radiation is very intense, with a daily average of over 400 Wm^{-2} for the same period, the

maximum for both hemispheres during the summer months excluding the South Pole.

The climatic regime of the Dry Central Andes is clearly different from that of subtropical Andes of Bolivia and Peru, further north, characterised by convective intrusions of moist air masses from the Amazon basin during the summer (Vuille et al. 1998). Here the ablation session is well defined and characterised by long periods of clear and stable weather. This climatic setting is responsible for the formation of a very peculiar ablation morphology, the snow penitentes, common to all the central Andes and to other dry high mountains like the Pamirs (Lliboutry 1965, Kotlyakov and Lebedeva 1974).

Snow and ice penitentes

Penitentes were first described in the literature by Darwin (1839). On March 22, 1835 he had to squeeze his way through snowfields covered in penitentes near the Piuquenes Pass, on the way from Santiago de Chile to the Argentinian city of Mendoza, and reported the local belief (continuing to the present day) that they were formed by the strong winds of the Andes. These pinnacles of snow or ice (figure 3) grow over all glaciated and snow covered areas in the Dry Andes above 4,000 m (Lliboutry 1954a, Lliboutry 1954b, Lliboutry 1965). They range in size from a few cm to over five metres. (Lliboutry 1965, Naruse and Leiva 1997).

Fig. 3. Penitentes field on the middle section of the Loma Larga glacier, at about 4500 m a.s.l. The whole glacier above 4000 m is covered in these snow pinnacles, which difficult the movement of mountaineers and researches and alters the surface energy balance of the glacier. On the right photograph is a detail of penitentes about 2 m in height.

Lliboutry (1954a, 1954b, 1965) noted that the key climatic condition for the differential ablation that leads to the formation of penitentes is that dew point is always below zero. Thus, snow will sublimate, which requires higher energy input than melting. Once the process of differential ablation starts, the surface geometry of the evolving penitente produces a positive feedback mechanism, and radiation is trapped by multiple reflections between the walls. The hollows become almost a black body for radiation (Lliboutry 1954a), while decreased wind leads to air saturation, increasing dew point temperature and the onset of melting. In this way peaks, where mass loss is only due to sublimation, will remain, as well as the steep walls, which intercept only a minimum of solar radiation. In the troughs ablation is enhanced, leading to a downward growth of penitentes. A mathematical model of the process has been developed by Betterton (2001), although the physical processes at the initial stage of penitente growth, from granular snow to micropenitentes, still remain unclear.

Methodology

Meteorological data collected at two sites in the Andes by an automatic weather station was used to model the energy balance and the relative importance of its components. A summary of the instrumentation is given in table 2. The model is a distributed model of solar radiation which takes into account the spatial variation both in atmospheric transmittance and in diffuse reflected radiation due to surrounding topography. In this case we focus on the microscale, to assess the effect of ablation morphology on the whole energy balance. For a correct estimation

Table 2. Instruments used for measuring air temperature, relative humidity, snow temperature, incoming and outgoing shortwave radiation, wind speed and wind direction.

	T_a	RH	T_s	SW↓	SW↑	$\bar{u}$	u_{xy}
sensor	Vaisala 50Y		107 Thermistor	Kipp&Zonen CM3		RM Young 05103	
range	-40 to 60°C	0 to 100%	-40 to 60°C	305–2800 nm		0-60ms^{-1}	360°
accuracy	±0.5°C	2%	±0.5°C	10%		±0.3 ms^{-1}	3%

of the influence of surrounding land cover on reflected diffuse radiation, whether snow free or snow covered, a novel technique using terrestrial photography was developed (Corripio 2003a, Corripio 2003b). This consists of georeferencing oblique photographs to a digital elevation model (DEM) and defining a mapping function between the information contained in a given pixel of the image and the corresponding cell of the DEM. This allows a simple estimation of the spatial variation in albedo and thus the influence of the surrounding land cover to be taken into account. This technique depends on the availability of digital elevation models and relies on the identification of accurate ground control points (GCPs). The procedure was not fully

developed until after the field campaign, but in order to illustrate its application to mountain terrain, a example for an Alpine glacier is given in figure 4.

Fig. 4. Example of the technique used to estimate the ratio of snow cover and the spatial distribution of albedo, in this case applied to an Alpine glacier, Haut Glacier d'Arolla. On the left photograph the perspective projection of the DEM appears as red dots, and from these, the georeferenced map of reflectance values on the right image is produced.

Energy balance model

The energy fluxes at the surface of the glacier can be expressed as:

$$Q = I_G(1 - \alpha) + L \downarrow - L \uparrow + H + L_e E \ , \tag{1}$$

where I_G is global shortwave radiation, α is snow albedo, L is longwave radiation, arrows indicating incoming or outgoing, H and $L_e E$ are sensible and latent turbulent fluxes with the atmosphere. Note that neither convective nor advective heat transfer within the snow pack was considered. However, the temperature at 1 m below the snow surface was measured on the lower AWS with a thermistor and found very stable, with a mean value of -0.13° C and a standard deviation of 0.0023, suggesting that most variation in temperature within the snowpack is the result of diffusion from the surface, with little or no heat fluxes from internal layers in accordance with other studies of temperate glaciers during the ablation season (Arnold et al. 1996, Obleitner 2000).

Shortwave radiation

The global shortwave radiation was modelled in the following way:

$$I_G = r^2 I_{sc} \tau_i (F_t + F_{sk} + F_{ms} + F_{sn}), \tag{2}$$

where I_{sc} is the solar constant or 1367 Wm^2; r^2 is the reciprocal of the square of the radius vector of the earth, or correction for the eccentricity of the earth's orbit, which is calculated using Fourier series derived by Spencer (1971); and τ_i represents atmospheric transmittance functions, both for diffuse and direct radiation, which take into account Rayleigh scattering, transmittance by ozone, by uniformly mixed gases, by water vapour and by aerosols, and are computed following a parametric model by Iqbal (1983). The τ–functions incorporate the relative optical path length and pressure corrected air mass, depending on solar zenith angle and altitude. Further updates to Iqbal's model are introduced for the calculation of precipitable water, following Prata (1996) and for ozone layer thickness, which is taken from the NASA Total Ozone Mapping Spectrometer dataset (TOMS–EP 2001). The F–factors are corrections for direct radiation with respect to its angle of incidence (F_t), for diffuse radiation (F_{sk}), multiple scattering (F_{ms}) and reflected radiation by, both snow covered and snow free surrounding terrain (F_{sn})). The F-terms take into account the horizon obstruction or sky view factor (f_v, Equation 6). They are computed in a slightly modified way from Greuell et al. (1997) as explained by Corripio (2003b), with terrain and solar parameters such as vector normal to the surface, shading, horizon configuration and solar vector calculated after Corripio (2003c).

The results of the model, compared with measured radiation on a clear day are shown in figure 5, where the differences between modelled and measured data were smaller than the nominal pyranometer accuracy (10%). In this case the valley is uniformly covered in snow and runs east to west, for different configurations there is a small error introduced by the necessary simplification and symmetry assumption of the terrain configuration parameters.

The albedo at the upper station was fairly constant, with an average value of 0.44 and a standard deviation of 0.07. Its decrease was only 4% over a month. An unusual pattern was observed at the upper AWS in the last hours of the afternoon, when the albedo value rose sharply to almost 1.0. This could be an artifact due to differential shading. Another possible explanation for this behaviour is an increase in reflected diffuse radiation as the sun hit the penitentes' wall from the west at a very low angle. The fact that the increase in albedo happens after 18:00 h, when the solar azimuth enters the southwestern quadrant, adds support to this hypothesis, although the causes are not clear yet.

Long wave radiation

The incoming long wave radiation depends on the temperature and composition of the overlying atmosphere, and in mountainous terrain the surrounding relief and snow cover will have an important effect on the total radiative budget (Olyphant 1986). The atmospheric component was calculated following Prata (1996), a formulation that gives the best results according to a survey by Dilley and O'Brien (1998), especially for dry atmospheres as is the case in the Andes.

$$L \downarrow = \left(1 - (1 + \omega_p)\, e^{-(1.2 + 3\omega_p)^{0.5}}\right) \sigma T_a^4, \tag{3}$$
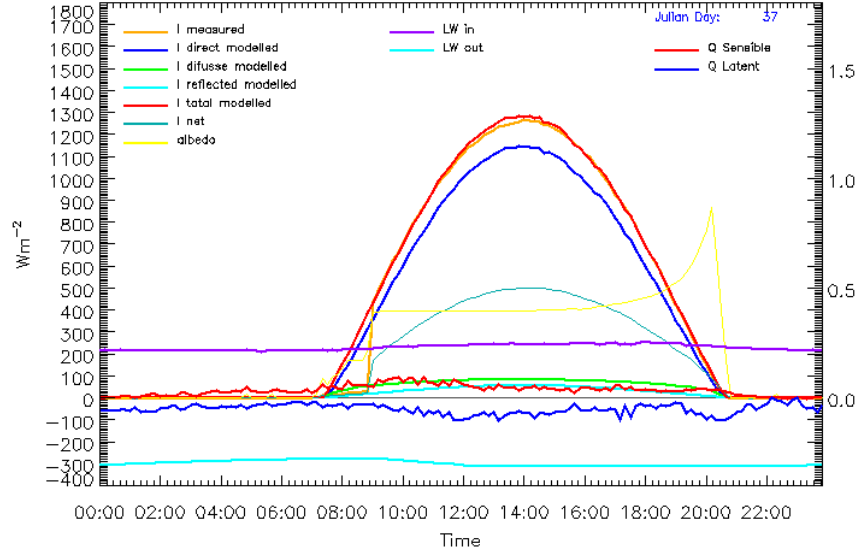
Fig. 5. Energy fluxes on a clear day on Loma Larga glacier, 4667 m a.s.l. DOY 37, 6th of February. Note the increasing albedo in the afternoon, an explanatory hypothesis is given in the text.

where T_a is air temperature (K) at screen level, σ is the Stephan-Boltzman constant and precipitable water (ω_p) is calculated as $\omega_p = 46.5\, e_0/T_a$, an empirical equation given by Prata (1996) that is the best fit to extensive data from radiosonde stations around the world, with e_0 the actual vapor pressure, calculated from measured relative humidity and from the saturation vapour pressure calculated using Lowe's (1977) polynomials.

The outgoing longwave radiation is:

$$L \uparrow = \epsilon \sigma T_s^4, \tag{4}$$

where ϵ is snow emissivity, taken as 0.99, and T_s is snow surface temperature.

The value of $L \downarrow$ is further modified according to the horizon configuration or sky view factor (f_v, Equation 6) and the snow cover ratio of surrounding ground as

$$L' \downarrow = L \downarrow f_v + L \uparrow (1 - f_v). \tag{5}$$

Turbulent fluxes

For the calculation of the turbulent fluxes, the Monin-Obukhov similarity theory was followed, as formulated by Brutsaert (1982). This method calculates heat and vapour transfer from their gradients between surface and measurement heights, taking into

consideration wind speed, air density, stability correction, etc., and accounts for the surface roughness by introducing an aerodynamic roughness length, z_0.

A standard approach for the computation of the roughness length for momentum is to extrapolate the profiles of wind speed under neutral conditions to the level where wind speed equals zero (Stull 1988, Munro 1989, Greuell and Smeets 2001). However, this procedure requires measurements at at least two levels and is very sensitive to instrument errors. Therefore the roughness for the lower site was selected from published mean values for melting snow (Marks and Dozier 1992, Morris 1989, Greuell and Smeets 2001), and it was calculated from microtopographical measurements for the upper site. This upper site is covered in large penitentes, sometimes over 1.5 m in height (figure 3), which results in a very long roughness length. It was calculated as $z_0/h = 0.5\lambda$, where h is the roughness element height and λ is the frontal area index or vertical silhouette area per unit ground area (Lettau 1969). Data from wind tunnel experiments and atmospheric obervations shows that z_0/h increases linearly with λ for $\lambda < \lambda_{max}$ (Raupach 1992). The precise form of this function and the value of λ_{max} depends on the geometry of the roughness elements, but the above linear relationship was found satisfactory for very rough snow surfaces on Vatnajökull, Iceland, by Smeets et al. (1999). For the present study, with an average penitente height of 1.35 m, separated about 0.8 m, the mean value of z_0 was found to be 20 cm. The frontal area index will change depending on wind direction, and so will do the surface roughness length, sometimes to a very large scale (Jackson and Carroll 1977), however, wind direction was observed to be fairly constant, either upvalley or downvalley, which justify the selected profile. Values for turbulent fluxes plotted on figure 5 correspond to this z_0 value. The transfer mechanisms of momentum and of other scalar admixtures are different at the surface, and consequently the roughness lengths have different values for momentum, water vapour and heat, which were calculated following Andreas (1987).

Modelling the surface microtopography

To assess the effect of the surface ablation morphology on the interception of solar radiation and on the long wave radiative budget, a high resolution digital elevation model of the surface with 1 cm grid cell spacing was created, and the solar radiative and longwave models applied to it. The turbulent heat transfer was considered at the overall scale, but it is expected that sublimation and cooling is more intense on the peaks and on the wind side. Although some effort has been made in determining drag partition on rough surfaces (Raupach 1992), it was only for momentum transfer, and it would be desirable to get more detailed observations on real snow surfaces before extrapolating any modelling results.

The DEM was created according to measured penitente distribution and size, with an average height of 1.35 m and wavelength of 0.80 m. To add more realism, the base of the troughs was made flat, as there is frequent melting and even small water ponds in these areas. A smoothing filter was passed over the whole surface to

avoid unrealistically sharp angles, but resulted in excessive flattening of the peaks. The 'virtual' penitentes are concave and tilted $11°$ to the north, the sun direction in the southern hemisphere (note the arrows in figure figure 7). As real penitentes have overhanging surfaces, these can not be represented by a mathematical function, which requires a single z–value for every (x,y) pair. By rotating the reference system by an equivalent angle, we can build the DEM with no overhanging surfaces, and then rotate the world according to this new reference system. For the calculation of solar irradiation on the penitentes surface (figure 7) we only need to rotate the sun vector through the original reference system an opposite angle by applying the appropriate rotational matrices.

The sky view factor was computed for every grid cell as the finite sum:

$$f_v = \sum_{\varphi=0}^{2\pi} \pi \cos^2 \theta \frac{\Delta\varphi}{2\pi} \qquad (6)$$

where θ is the local horizon angle, including the slope of the cell itself, for a given azimuth, φ. This represents the ratio of the area of a projected circle, corresponding to the visible part of the hemisphere to the area of a circle of unit radius corresponding to the whole hemisphere. For a more detailed explanation see for example: Nuñez (1980), Dozier (1981, 1990), or Corripio (2003c, 2003a)

The model calculated angle of incidence of the direct beam, shadows, diffuse reflected radiation and diffuse radiation from the sky. For a detailed discussion see Greuell et al. (1997, appendix) and Corripio (2003c). Reflected radiation was computed for five multiple reflections, which accounts for more than 97% of the energy from this source. Only even reflections were computed, as odd reflections are 'reflected–out' (Peterson et al. 1985). The modified incoming longwave radiation is a function of the skyview factor, its value outside the penitentes layer and the longwave emission of surrounding walls.

Results and discussion

The recorded meteorological variables are summarised in tables 3 and 4. The most remarkable aspect is the very low relative humidity. High values were normally associated with the presence of clouds, sometimes enveloping the AWS. Relative humidity follows a diurnal cycle, with maxima due to nocturnal cooling and minima normally related to katabatic winds. Winds were light to moderate and fairly constant. Incoming solar radiation was very intense, with average values close to those of perfectly clear days and peaks exceeding 1700 Wm^{-2} at the upper AWS. These peaks were higher than the exoatmospheric radiation and were probably caused by enhanced downward flux due to forward scattering of light by large cumulonimbus. Albedo was fairly constant during the whole measurement period, and typically 8% lower on the upper station, where the site was completely covered in penitentes. The calculated dew point was well below zero, with very rare exceptions.

Table 3. Recorded meteorological variables and calculated dew point on both glaciers at different times of the day. Noon is about two hours around the daily peak of maximum shortwave radiation, sunrise and sunset are extended two hours after and before the respective events, and night correspond to the period where there is no incoming shor-twave radiation. Note that although dew point is a function of temperature and humidity, the recorded variables, its calculated value is given to stress the meteorological conditions necessary for the formation of penitentes as pointed out by Lliboutry (1954b).

Juncal Norte Glacier (3335 m a.s.l.)												
Time	noon				sunrise -set				night			
	min	**mean**	max	σ	min	**mean**	max	σ	min	**mean**	max	σ
T °C	5.2	**11.2**	17.3	2.4	1.3	**7.2**	14.3	2.5	1.2	**5.7**	10.3	2.1
RH %	10.6	**21.8**	51.4	6.5	10.4	**37.1**	75.4	13.7	14.7	**44.6**	80.3	14.4
u ms^{-1}	0.4	**13.6**	5.0	2.0	0.1	**3.9**	11.3	1.9	0.1	**3.2**	6.5	1.2
Dew Point °C	-18.8	**-10.4**	-0.6	3.5	-19.3	**-7.3**	1.1	4.3	-16.5	**-6.0**	1.6	4.0
Loma Larga Glacier (4667 m a.s.l.)												
T °C	5.2	**11.2**	17.3	2.4	1.3	**7.2**	14.3	2.5	1.2	**5.7**	10.3	2.1
RH %	10.6	**21.8**	51.4	6.5	10.4	**37.1**	75.4	13.7	14.7	**44.6**	80.3	14.4
u ms^{-1}	0.4	**13.6**	5.0	2.0	0.1	**3.9**	11.3	1.9	0.1	**3.2**	6.5	1.2
Dew Point °C	-18.8	**-10.4**	-0.6	3.5	-19.3	**-7.3**	1.1	4.3	-16.5	**-6.0**	1.6	4.0

Table 4. Short wave radiation and derived albedo at Juncal NorteGlacier (3335 m) and Loma Larga Glacier (4667 m)

	Juncal Norte Glacier			Loma Larga glacier		
	SW↓ Wm^{-2}	SW↑ Wm^{-2}	albedo %	SW↓ Wm^{-2}	SW↑ Wm^{-2}	albedo %
min	—	—	—	—	—	—
mean	**353**	**184**	**0.52**	**383**	**163**	**0.44**
max	1564	810	0.70	1727	737	0.65

It should be pointed out that there were not reliable measurements of ablation in the area of study. This is not a simple task, as the volumetric change of the penitentes should be measured, besides their growth and lowering. However, to gain some confidence in the modelled data, the energy balance model was applied to the meteorological data recorded on the ablation area at the Haut Glacier d'Arolla, during the ETH summer campaign 2001. The modelled ablation was then compared to ablation measured by a sonic gauge. The results show good agreement, as illustrated in figure 6. It is interesting to point out the differences in the turbulent fluxes between the Alpine and the Andean glaciers. In the Alps net turbulent flux was always positive: $16\,\mathrm{Wm}^{-2}$ mean value in the period corresponding to the plotted data, from 19 June to 5 July, with a standard deviation of 29.5. In general, large negative fluxes were associated to precipitation events, where sensible flux was also negative, while in the Andes large negative fluxes were associated with intense evaporation.

The energy balance model applied to the microtopography DEM was run for several clear days with ten minute time steps to asses the effect of penitentes on the interception of solar radiation. The results for day 37 are shown in figure 7. The maximum total daily value is 490 Wm^{-2}, while the mean value is only 207 Wm^{-2}. The histogram of values shows a bimodal distribution with two peaks (248 and 156 Wm^{-2}) corresponding to the north and south facing walls. The same day on a flat surface the modelled (and measured) radiation was 435 Wm^{-2} (418). The mean values for the summer solstice (21 December) were 230 and 486 Wm^{-2} for the penitentes and a flat surface respectively. Although not shown, an inspection of the results for diffuse and reflected radiation reveals that the latter increases downwards and the former increases upwards, with a maximum at the peaks.

Net longwave radiation increased its mean value from -77 Wm^{-2} on a flat surface to -38 Wm^{-2} on the penitentes, due to emitted radiation from the surrounding snow walls. Turbulent fluxes decreased their net value from -17 to -28 Wm^{-2} on average (table 5). These values are averages for all grid cells, however surface area is different according to the slope of the cell, and total area is increased on a rough surface, in this case by a factor of 2.8. On the larger scale we have to assume the conservation of radiative fluxes, and therefore the main change in the overall energy balance is brought about by the increased turbulent fluxes due to increased roughness. This change represents about 2.85 mm of water equivalent melt (mmwe) decrease per day or 342 mmwe for the four principal months of the ablation season. The partition of the energy balance components on the altered snow surface is also important. Thus, the penitentes' walls receive about half of the incoming solar radiation with
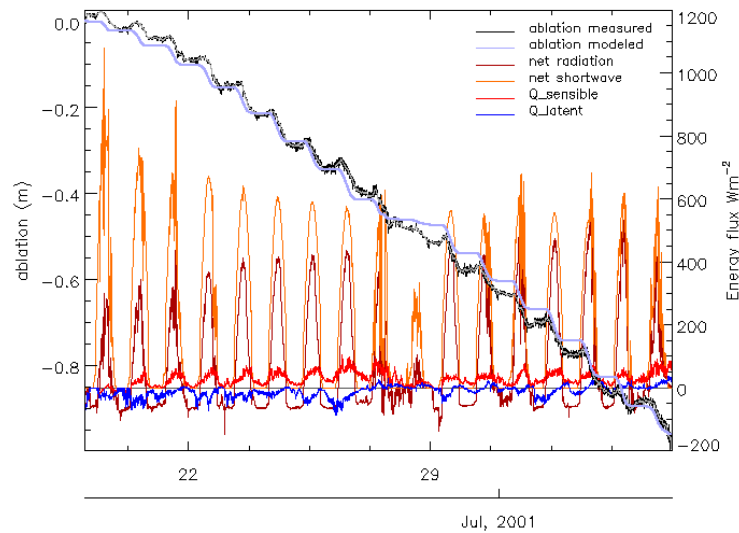

Fig. 6. Recorded solar radiation, estimated turbulent fluxes, and recorded and estimated snow ablation on the Haut Glacier d'Arolla from 19 June to 5 July 2001.

respect to a flat surface. This compensates for the increase in longwave radiation and keeps the penitentes' walls generally frozen and dry, while melting occurs only at the bottom of the troughs. The localized melting favours percolation of water, with almost no supraglacial drainage, which in turn reduces loss of water by further evaporation. This corresponds well with the observed situation, although small streams may form lower down and later in the ablation season, as seen on the Horcones glacier on Aconcagua in a different year. Nonetheless these streams are much smaller than supraglacial rivers observed in the Alps.

Table 5. Energy balance partition for flat snow and penitentes (Wm^{-2})

	SW↓	SWnet	LWnet	Net Turbulent Flux	Total
Flat snow	435	209	-77	-17	115
Penitentes (mean)	238	133	-38	-28	67

Sensitivity of energy balance and implications

This work has addressed the formation of penitentes through an experimental and modelling campaign in the Andes. Penitentes are a unique and complex form which result from a relatively narrow band of meteorological conditions. Thus, any change in climate is likely to have implications for the formation of penitentes, and thus in turn the mass balance of glaciers as their buffering effect on snow melt, as discussed in the previous section, is reduced.

A simple study of the sensitivity of the energy balance to different parameters and its variation with height was carried out. This is represented in figure 8. We can observe a minimum of the net energy balance at about 4600 m a.s.l., which corresponds well with the maximum extension of penitentes. The shape of the curve is relatively sensitive to initial temperature and relative humidity and very sensitive
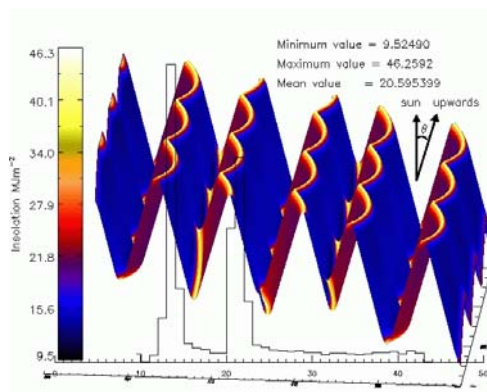

Fig. 7. Insolation on penitentes for the 37th day of the year, corresponding to values in figure 5. Superimposed is the histogram of cell values, clearly showing a bimodal distribution of insolation values corresponding to the north facing and south facing slopes. The reference system is rotated an angle θ so that the vertical is the direction of the sun at midday on the summer solstice.

to wind speed. Wind speed was fairly constant and moderate to light at the upper AWS, with values that are very similar to recorded values in a previous campaign in the Argentinian Andes at similar latitude and height. Increased wind speed decreases dramatically the net energy balance and would prevent the formation of penitentes, as the turbulent fluxes are proportional to roughness. This was observed on the upper section of the Juncal glacier, where wind is higher on unsheltered slopes and snow is less metamorphosed and relatively smooth. However, penitentes were found not far below the summit of Nevado Juncal (6100 m) in a very sheltered location. A similar situation was observed on Cerro Aconcagua, where the snow ablated into penitentes up to an altitude of 5800 m except on the very wind exposed eastern section (Polish glacier), where flatter snow or bare ice existed. Running the model with a dry adiabatic lapse rate, as may be expected under a katabatic wind regime, results in a shift of the minimum in energy balance to a lower altitude. The same situation could be expected earlier in the season, when air temperature is lower. Observations on Juncal glacier confirmed this, the lower line of penitentes formation migrated upwards from about 3700 m in early December to about 4000 m later in the season. Small penitentes formed at lower elevations gradually became wet, rounded and disappeared over a period of a few weeks.
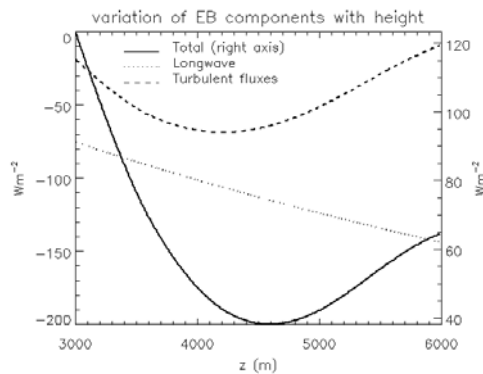

Fig. 8. Variation of the energy balance components with height for mean recorded values at the lower AWS (3335 m a.s.l.) applying a standard lapse rate (-0.0065Km^{-1}). Shortwave global radiation is modified primarily by albedo, which in this case was simplified to a constant value.

Through this set of experimental and modelled data we can make a number of observations about the impact of changes in meteorological variables:

- Increased humidity will hinder the formation of penitentes, both by decreasing the latent heat flux and increasing the net long wave radiation
- Increased temperature will shift upwards the lower limit of penitentes formation
- Stronger circulation with increased wind speeds will decrease or suppress penitentes formation.

This initial sensitivity study does not allow us to comment on the likely implications of climate change on penitentes and subsequent influences on glacier energy and mass balance. Rather, it demonstrates that penitentes are sensitive to changes

in meteorological parameters and that the model developed allows us to form some initial hypotheses about the likely impacts. Further work, including the extensive collection of field data in stable and unstable atmospheric conditions should shed further light on these processes.

As we have seen, the formation of penitentes occurs within a narrow band of climatic conditions, and their presence provides information on seasonal trends, a point already stressed by Kotlyakov and Lebedeva (1974), thus, one direct application of the relationship between snow surface morphology and climate is the potential use of remote sensing for assessing seasonal climatic conditions. The increased roughness of penitentes is potentially detectable using SAR polarimetry, while changes in albedo may identify the differences between flat snow and penitentes areas through the use of optical remote sensing. To exploit the full potential of this relationship a better knowledge of the initial stages in the formation of micropenitentes is needed, and that was beyond the scope of the present work. Far more detailed micrometeorological measurements in the field, or the replication of the process in a cold laboratory under controlled circumstances would be necessary to gain full insight into this process of snow ablation.

Conclusions

The climatic characteristics of the Dry Central Andes – low humidity and high solar radiation inputs in stable summers coupled with high evaporation rates and strong radiative cooling – results in a unique snow ablation morphology: penitentes. Modelling and field data suggest that any changes in the meteorological conditions during the initital stages of growth of penitentes early in the ablation season, for example, increased humidity, longwave radiation or stronger winds may supress or hinder their formation. Since the growth of penitentes is self supported in part by a positive feedback mechanism, the consequences of a small change in meteorological conditions may result in a disproportionate change in overall ablation. Modelling work suggests that penitentes enhance conservation of snow cover and the consequences of their loss might be increased ablation over the whole season, decreased glacier mass balance and faster depletion of water resources. Given the critical nature of snow and ice melt in relation to water resources for human consumption and agricultural resources in the Central Andes any potential change is worthy of further research.

Acknowledgements

List of symbols

Symbol	Definition
e_0	vapour pressure (hPa)
E	evaporation (kg)
EL_e	latent turbulent heat flux (Wm^2)
f_v	skyview factor (dimensionless)
F_t	correction term for the angle of incidence of sun on the slope (dimensionless)
F_{ms}	correction term for diffuse radiation due to multiple scattering between ground and sky (dimensionless)
F_{sk}	correction term for diffuse radiation from the sky (dimensionless)
h	roughness element height (m)
H	sensible turbulent flux per unit area (Wm^2)
I_{sc}	solar constant (mean value: 1367 Wm^2)
I_G	incoming global solar radiation flux (Wm^2)
$L\downarrow$	long–wave downward radiative flux (Wm^2)
$L\uparrow$	long–wave upward radiative flux (Wm^2)
$L'\downarrow$	long–wave radiative flux reflected from surrounding slopes (Wm^2)
L_e	latent heat of evaporation/sublimation (J kg^{-1})
r^2	reciprocal of the square of the radius vector of the earth (dimensionless)
RH	relative humidity (dimensionless)
$SW\downarrow$	short–wave downward radiative flux (Wm^2)
$SW\uparrow$	short–wave upward radiative flux (Wm^2)
T_a	air temperature at screen level (K)
T_s	snow surface temperature (K)
$\bar{u}$	mean wind speed (ms^{-1})
α	albedo (dimensionless)
ε	emissivity (dimensionless)
λ	frontal area index (dimensionless)
σ	Stephan-Boltzman constant (5.6696E-8 Wm$^{-2}K^{-4}$)
θ	local horizon angle (radians)
φ	azimuth (radians)
ω_p	precipitable water (cm)

References

Andreas, E. L.: 1987, A theory for the scalar roughness and the scalar transfer coefficients over snow and sea ice, *Boundary layer Meteorology* **38**, 159–184.

Arnold, N. S., Willis, I. C., Sharp, M. J., Richards, K. S. and Lawson, M. J.: 1996, A distributed surface energy–balance model for a small valley glacier, *Journal of Glaciology* **42**(140), 77–89.

Betterton, M. D.: 2001, Theory of structure formation in snowfields motivated by penitentes, suncups, and dirt cones, *Physical Review E* **63**(056129), 12 pages.
    *http://prola.aps.org/

Brutsaert, W.: 1982, *Evaporation into the atmosphere : theory, history, and applications*, 1984 edn, Reidel, Dordrecht.

Corripio, J. G.: 2003a, *Modelling the energy balance of high altitude glacierised basins in the Central Andes*, PhD thesis, University of Edinburgh. Unpublished.

Corripio, J. G.: 2003b, Snow surface albedo estimation using terrestrial photography, *International Journal of Remote Sensing* . Submitted.

Corripio, J. G.: 2003c, Vectorial algebra algorithms for calculating terrain parameters from DEMs and the position of the sun for solar radiation modelling in mountainous terrain, *International Journal of Geographical Information Science* **17**(1), 1–23.

Darwin, C.: 1839, *Journal of researches into the geology and natural history of the various countries visited by H. M. S. Beagle, under the command of Captain Fitz Roy, R.N., 1832 to 1836*, H. Colburn, London.

Dilley, A. C. and O'Brien, M. O.: 1998, Estimating downward clear sky long–wave irradiance at the surface from screen temperature and precipitable water, *Quarterly Journal of the Royal Meteorological Society* **124**(549), 1391–1401.

Dozier, J., Bruno, J. and Downey, P.: 1981, A faster solution to the horizon problem, *Computers & Geosciences* **7**, 145–151.

Dozier, J. and Frew, J.: 1990, Rapid calculation of terrain parameters for radiation modelling from digital elevation data, *IEEE Transactions on Geoscience and Remote Sensing* **28**(5), 963–969.

Greuell, W., Knap, W. H. and Smeets, P. C.: 1997, Elevational changes in meteorological variables along a midlatitude glacier during summer, *Journal of Geophysical Research* **102**(D22), 25941–25954.

Greuell, W. and Smeets, P.: 2001, Variations with elevation in the surface energy balance on the Pasterze, Austria, *Journal of Geophysical Research* **106**(D23), 31,717–31,727.

Iqbal, M.: 1983, *An Introduction to Solar Radiation*, Academic Press, Toronto.

Jackson, B. and Carroll, J.: 1977, Aerodynamic roughness as a function of wind direction over asymmetric surface elements, *Boundary Layer Meteorology* **14**, 323–330.

Kotlyakov, V. M. and Lebedeva, I. M.: 1974, Nieve and ice penitentes, their way of formation and indicative significance, *Zeitschrift für Gletscherkunde und Glazialgeologie* **Bd X**, 111–127.

Lettau, H.: 1969, Note on aerodynamic roughness-parameter estimation on the basis of roughness-element description, *Journal of Applied Meteorology* **8**, 828–832.

Liniger, H., Weingartner, R. and Grosjean, M. (eds): 1998, *Mountains of the World – Water Towers for the 21st Century*, Mountain Agenda for the Commission on Sustainable Development (CSD), University of Bern.

Lliboutry, L.: 1954a, Le Massif du Nevado Juncal ses penitentes et ses glaciers, *Revue de Géographie Alpine* **42**, 465–495.

Lliboutry, L.: 1954b, The origin of penitentes, *Journal of Glaciology* **2**(15), 331–338.

Lliboutry, L.: 1965, *Traité de Glaciologie*, Vol. I & II, Masson, Paris.

Lliboutry, L.: 1998, Glaciers of the Dry Andes, *in* R. S. J. Williams and J. G. Ferrigno (eds), *Satellite Image Atlas of Glaciers of the World SOUTH AMERICA*, United States Geological Survey Professional Paper 1386–I.
    *http://pubs.usgs.gov/prof/p1386i/index.html

Lowe, P. R.: 1977, An approximating polynomial for the computation of saturation vapor pressure, *Journal of Applied Meteorology* **16**, 100–103.

Marks, D. and Dozier, J.: 1992, Climate and energy exchange at the snow surface in the alpine region of the Sierra Nevada. 2. Snow cover energy balance, *Water Resources Research* **28**(11), 3043–3054.

Morris, E. M.: 1989, Turbulent transfer over snow and ice, *Journal of Hydrology* **105**, 205–223.

Munro, D. S.: 1989, Surface roughness and bulk heat transfer on a glacier: comparison with eddy correlation, *Journal of Glaciology* **35**(121), 343–348.

Naruse, R. and Leiva, J. C.: 1997, Preliminary study on the shape of snow penitents at Piloto Glacier, the Central Andes, *Bulletin of Glacier Research* **15**, 99–104.

Nuñez, M.: 1980, The calculation of solar and net radiation in mountainous terrain (Risdon, Tasmania), *Journal of Biogeography* **7**(2), 173–186.

Obleitner, F.: 2000, The energy budget of snow and ice at Breidamerkurjökull, Vatnajökull, Iceland, *Boundary Layer Meteorology* **97**, 385–410.

Olyphant, G. A.: 1986, Longwave radiation in mountainous areas and its influence on the energy balance of alpine snowfields, *Water Resources Research* **22**(1), 62–66.

Peterson, W. A., Dirmhirn, I. and Hurst, R. L.: 1985, A theoretical model to determine solar and diffuse irradiance in valleys, *Solar Energy* **35**(6), 503–510.

Prata, A. J.: 1996, A new long–wave formula for estimating downward clear–sky radiation at the surface, *Quarterly Journal of the Royal Meteorological Society* **122**, 1127–1151.

Raupach, M. R.: 1992, Drag and drag partition on rough surfaces, *Boundary Layer Meteorology* **60**, 375–395.

Schwerdtfeger, W.: 1976, *World survey of climatology. Climates of Central and South America*, Elsevier, Amsterdam.

Smeets, C., Duynkerke, P. and Vugts, H.: 1999, Observed wind profiles and turbulence over an ice surface with changing surface roughness, *Boundary Layer Meteorology* **92**, 101–123.

Spencer, J. W.: 1971, Fourier series representation of the position of the sun, *Search* **2**, 172.

Stull, R.: 1988, *An introduction to boundary layer meteorology*, Kluwer Academic, Dordrecht.

TOMS–EP: 2001, Total Ozone Mapping Spectrometer–Earth Probe data sets.
    *http://toms.gsfc.nasa.gov/eptoms/ep.html

Vuille, M., Hardy, D. R., Braun, C., Keimig, F. and R Bradley, R.: 1998, Atmospheric circulation anomalies associated with 1996/1997 summer precipitation events on Sajama Ice Cap, Bolivia, *Journal of Geophysical Research* **103**(D10), 11191– 11204.